Independent Operation of DFIG-Based WECS Using Resonant Feedback Compensators Under Unbalanced Grid Voltage Conditions

Heng Nian, *Member, IEEE*, Peng Cheng, and Z. Q. Zhu, *Fellow, IEEE*

***Abstract*—This paper presents an independent operation of the rotor-side converter (RSC) and grid-side converter (GSC) for a doubly fed induction generator (DFIG)-based wind energy conversion system under unbalanced grid voltage conditions. In this paper, the RSC is controlled to achieve four different control targets, including balanced stator current, sinusoidal rotor current, smooth stator active and reactive powers, and constant DFIG electromagnetic torque. The GSC is commanded to keep the dc voltage at a constant value. Additional feedback compensators using resonant regulators for the RSC are employed, and the decompositions of the positive and negative sequence components and calculations of the rotor negative current references can be avoided. Another similar compensator is used in the GSC to suppress the dc voltage fluctuates and remove the GSC reactive power oscillations without the stator or rotor power information. The proposed method can make the RSC and GSC available to an independent operation with a simple implementation for higher reliability. The experimental results demonstrate the effectiveness of the proposed control strategy for both the RSC and GSC under unbalanced grid voltage conditions.**

***Index Terms*—Doubly fed induction generator (DFIG), independent operation, resonant regulator, unbalanced grid voltage, wind energy conversion system (WECS).**

I. Introduction

NOWADAYS, wind power generations have been growing rapidly all over the world and have become one of the most promising renewable generation technologies. Among the different types of the wind energy conversion system (WECS), doubly fed induction generator (DFIG)-based WECSs, as shown in Fig. 1, have gained the increasing proportion due to the outstanding advantages, including the variable speed constant frequency operation, four-quadrant active and reactive power capabilities, smaller converters rating around 30% of the generator rating, lower cost and power losses, compared with fixed-speed induction generators and synchronous generators [1]–[4].

Manuscript received April 9, 2014; revised May 28, 2014; accepted July 27, 2014. Date of publication August 7, 2014; date of current version February 13, 2015. This work was supported in part by the China National Science and Technology Support Program under Project 2011AA050204, and the National Natural Science Foundation of China under Project 51277159. Recommended for publication by Associate Editor M. Liserre.

H. Nian and P. Cheng are with the College of Electrical Engineering, Zhejiang University, Hangzhou 310027, China (e-mail: nianheng@zju.edu.cn; cheng_peng@zju.edu.cn).

Z. Q. Zhu is with the Department of Electronic and Electrical Engineering, University of Sheffield, Sheffield S1 3JD, U.K. (e-mail: z.q.zhu@sheffield.ac.uk).

Color versions of one or more of the figures in this paper are available online at http://ieeexplore.ieee.org.

Digital Object Identifier 10.1109/TPEL.2014.2346190

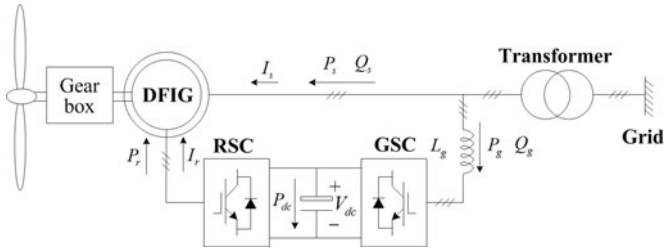

Fig. 1. Configuration of DFIG-based WECS.

Normally, DFIG-based WECSs are installed in the remote areas where the rural grids are weak and voltage imbalances often occur due to the unbalanced loads and the asymmetric grid fault. As the grid imbalance appears, the negative sequence flux linkages and currents arise in both the stator and rotor windings [5]–[8], which results in the significant double frequency ripples in the electromagnetic torque and may shorten the mechanical components lifetime. Besides, the oscillating power, flowing through the dc link between the grid-side converter (GSC) and rotor-side converter (RSC), causes the twice frequency voltage fluctuations in the dc capacitor [8]. As a result, DFIG-based generation systems without unbalanced voltage control might have to be disconnected from the grid, which is not accepted by the new grid code [9]–[11]. Thus, it is necessary that the DFIG-based WECSs should have the capability to operate under a certain steady-state voltage unbalance and endure the larger transient voltage imbalance without tripping.

The operation of the grid-connected DFIG system during network unbalance has been investigated in [6]–[8], [12]–[19]. In the traditional control scheme of DFIG systems, two proportional-integral (PI) controllers were applied in the current control loop on the basis of the decomposition of positive and negative sequence components in [6] and [17], where the current controllers were implemented in the positive and negative synchronous reference frames, respectively. Due to the time delay and control errors introduced by the decomposition of both the positive and negative sequence components, the system dynamic performance and stability might be degraded. In addition, it is necessary to decompose the measured signals to calculate the negative sequence current references even under ideal grid voltage conditions, which significantly increases the computational burden for the practical implementation. In [12] and [13], the decomposition processes in the control loop were removed by using resonant regulators.

The current control scheme consists of a PI regulator and a resonant (R) one tuned at the double grid frequency in the positive synchronous reference frame [12], or a proportional (P) regulator and a resonant (R) one tuned at the grid frequency in the stator stationary reference frame [13]. The different control targets during network unbalance, such as reducing current imbalances, reducing torque ripples, and removing power oscillations, were identified in [6], [12], and [13]. For these control targets, it is necessary to calculate the negative sequence current references based on the involved positive and negative sequential decomposition. In order to avoid the complicated negative sequence current reference calculation, the control reference of rotor voltage was calculated directly either from the calculated compensating currents [14] or from the torque ripples [15] to reduce torque ripples of DFIG. These two methods contain a band-pass filter followed by a lead-lag controller, which increase the design complexity and the computational burden for a DSP-based implementation.

Furthermore, when the DFIG system operates on the unbalanced grid, the double frequency fluctuations of dc voltage should be eliminated to reduce power losses and improve system reliability. In [16]–[19], the reduction of dc voltage fluctuates was discussed. The commanded current values for the GSC were calculated according to the real-time oscillating terms of either the rotor active power [16] or the stator active power [17]. By these coordinated strategies, the dc voltage fluctuates can be suppressed. However, the operation performance is highly dependent on the accuracy of the negative sequence current calculations based on the real-time power information from the RSC. To avoid these reference calculations, a direct power control strategy for DFIG systems was proposed in [18], where the electromagnetic power induced from the stator side was injected into the dc voltage control loop as a feed-forward term. However, in these coordinated strategies, the GSC requires the power information from the RSC, which means the RSC and GSC should be integrated into a whole, which is not beneficial for the independent operation of DFIG systems. In [19], a dc capacitor current control method using a negative sequence resonant controller was applied to the GSC control scheme, in which the dc voltage fluctuates can be reduced without additional hardware and power information from the RSC. However, the differential term of the dc voltage $V_{\rm dc}$ is involved in this method, which can amplify the high frequency noises and reduce the signal and noise ratio. Thus, it is necessary to investigate an entire control scheme to implement an independent operation with less computational burden and less system complex for DFIG systems under unbalanced grid voltage conditions.

This paper presents an independent control scheme using resonant feedback compensators for the RSC and GSC under unbalanced grid voltage conditions. This paper will be organized as follows. First, Section II describes the typical performance of DFIG-based systems under unbalanced grid voltage conditions. Then, the control schemes for both the RSC and GSC, using resonant feedback compensators in the positive synchronous reference frame, are introduced in Section III. The control performance analysis, containing the rejection capabilities and the dynamic responses, is given in Section IV. Experimental results are presented in Section V. Finally, Section VI summarizes the conclusions.

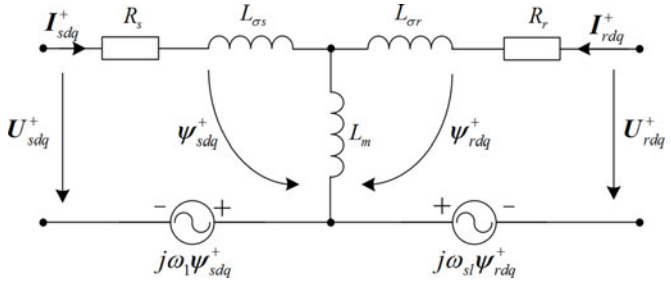

Fig. 2. DFIG equivalent circuit in the positive synchronous reference frame.

II. Mathematical Model of the DFIG System

In a DFIG-based generation system, the primary objective of the RSC is to control the average value of the stator active and reactive powers and the GSC keeps the dc voltage at a constant value. Since the detailed model of both the RSC and GSC under unbalanced grid condition has been studied in [6], [18], [21]–[22], a brief description is directly given in this section.

A. RSC (DFIG) Model

The DFIG equivalent circuit in the positive synchronous dq^+ reference frame is shown in Fig. 2, where the stator and rotor flux linkages can be expressed as, respectively

$$\boldsymbol{\psi}^+_{sdq} = L_s\boldsymbol{I}^+_{sdq} + L_m\boldsymbol{I}^+_{rdq} \tag{1}$$

$$\boldsymbol{\psi}^+_{rdq} = L_m\boldsymbol{I}^+_{sdq} + L_r\boldsymbol{I}^+_{rdq} \tag{2}$$

where $\boldsymbol{\psi}$ is the flux, $\boldsymbol{I}$ is the current, $L_s = L_m + L_{\sigma s}$ and $L_r = L_m + L_{\sigma r}$ are the self-inductances of stator and rotor windings, $L_{\delta s}$, $L_{\delta r}$, and L_m are stator and rotor leakage inductances and mutual inductance, superscripts $+$ represents the positive synchronous reference frame, subscripts *s* and *r* represent the stator and rotor, subscripts *d* and *q* represent components at the *d*–*q* axes, respectively.

According to Fig. 2, the stator and rotor voltages in the dq^+ reference frame can be expressed as

$$\boldsymbol{U}^+_{sdq} = R_s\boldsymbol{I}^+_{sdq} + \frac{d\boldsymbol{\psi}^+_{sdq}}{dt} + j\omega_1\boldsymbol{\psi}^+_{sdq} \tag{3}$$

$$\boldsymbol{U}^+_{rdq} = R_r\boldsymbol{I}^+_{rdq} + \frac{d\boldsymbol{\psi}^+_{rdq}}{dt} + j\omega_{sl}\boldsymbol{\psi}^+_{rdq} \tag{4}$$

where $\boldsymbol{U}$ is the voltage, R_s and R_r are stator and rotor resistances, respectively, ω_1 is synchronous angular speed, ω_r is rotor angular speed, and $\omega_{sl} = \omega_1 - \omega_r$ is slip angular speed.

From (1) to (4), the rotor voltage in the dq^+ reference frame can be expressed as

$$\boldsymbol{U}^+_{rdq} = \sigma L_r\frac{d\boldsymbol{I}^+_{rdq}}{dt} + \boldsymbol{E}_{rdq} \tag{5}$$

where $\sigma = 1 - L_m^2/(L_sL_r)$ is the leakage factor, and $\boldsymbol{E}_{rdq}$ is the equivalent rotor back electromagnetic force and given

as

$$\boldsymbol{E}_{rdq} = (R_r + \boldsymbol{j}\sigma L_r\omega_{sl})\boldsymbol{I}^+_{rdq} + \frac{L_m}{L_s}(\boldsymbol{U}^+_{sdq} - R_s\boldsymbol{I}^+_{sdq} - j\omega_r\boldsymbol{\psi}^+_{sdq}). \quad (6)$$

Under unbalanced grid voltage conditions, the stator active and reactive powers can be expressed as [6], [18]

$$S_s = P_s + \boldsymbol{j}Q_s = 1.5\,\boldsymbol{U}^+_{sdq} \times \hat{\boldsymbol{I}}^+_{sdq} \quad (7)$$

where superscripts $\wedge$ represents the conjugate complex, S_s, P_s, and Q_s represent the stator apparent, active and reactive powers, respectively

$$P_s = P_{sa} + P_{ss2}\sin(2\omega_1 t) + P_{sc2}\cos(2\omega_1 t) \quad (8a)$$

$$Q_s = Q_{sa} + Q_{ss2}\sin(2\omega_1 t) + Q_{sc2}\cos(2\omega_1 t) \quad (8b)$$

$$\begin{bmatrix} P_{sa} \\ Q_{sa} \\ P_{ss2} \\ P_{sc2} \\ Q_{ss2} \\ Q_{sc2} \end{bmatrix} = 1.5\frac{1}{\omega_1 L_s}\begin{bmatrix} U^+_{sd+} & U^+_{sq+} & U^-_{sd-} & U^-_{sq-} \\ U^+_{sq+} & -U^+_{sd+} & U^-_{sq-} & -U^-_{sd-} \\ U^-_{sq-} & -U^-_{sd-} & -U^+_{sq+} & U^+_{sd+} \\ U^-_{sd-} & U^-_{sq-} & U^+_{sd+} & U^+_{sq+} \\ -U^-_{sd-} & -U^-_{sq-} & U^+_{sd+} & U^+_{sq+} \\ U^-_{sq-} & -U^-_{sd-} & U^+_{sq+} & -U^+_{sd+} \end{bmatrix} \times \left(\begin{bmatrix} U^+_{sq+} \\ -U^+_{sd+} \\ -U^-_{sq-} \\ U^-_{sd-} \end{bmatrix} - \omega_1 L_m \begin{bmatrix} I^+_{rd+} \\ I^+_{rq+} \\ I^-_{rd-} \\ I^-_{rq-} \end{bmatrix} \right) \quad (8c)$$

where superscripts $+$ and $-$ represent the positive and negative synchronous reference frame, subscripts $+$ and $-$ represent the positive and negative sequence components, P_{sa}, P_{ss2}, and P_{sc2} represent the average, sine and cosine components of the stator active power, and Q_{sa}, Q_{ss2}, and Q_{sc2} represent the average, sine and cosine components of the stator reactive power, respectively.

Similarly, the electromagnetic torque can be expressed as [6], [18]

$$T_e = 1.5n_p\frac{L_m}{L_s}\mathrm{Re}[j\boldsymbol{\psi}^+_{sdq} \times \hat{\boldsymbol{I}}^+_{rdq}] \quad (9)$$

where n_p represents number of pole pairs, Re represents the real part, and T_e represents the electromagnetic torque

$$T_e = T_{ea} + T_{es2}\sin(2\omega_s t) + T_{ec2}\cos(2\omega_s t) \quad (10a)$$

$$\begin{bmatrix} T_{ea} \\ T_{es2} \\ T_{ec2} \end{bmatrix} = \frac{3}{2}n_p\frac{L_m}{L_s}\begin{bmatrix} -\psi^+_{sq+} & \psi^+_{sd+} & -\psi^-_{sq-} & \psi^-_{sd-} \\ \psi^-_{sd-} & \psi^-_{sq-} & -\psi^+_{sd+} & -\psi^+_{sq+} \\ -\psi^-_{sq-} & \psi^-_{sd-} & -\psi^+_{sq+} & \psi^+_{sd+} \end{bmatrix} \times \begin{bmatrix} I^+_{rd+} \\ I^+_{rq+} \\ I^-_{rd-} \\ I^-_{rq-} \end{bmatrix} \quad (10b)$$

where T_{ea}, T_{es2}, and T_{ec2} represent the average, sine and cosine components of the electromagnetic torque, respectively.

B. GSC Model

Under unbalanced grid voltage conditions, the GSC can be modeled by considering both the positive and negative sequence components, which is similar to the grid-connected voltage-source converter (VSC) [21], [22]. Thus, the GSC output voltage $\boldsymbol{U}^+_{gdq}$ can be represented in the positive synchronous dq^+ reference frame as follows:

$$\boldsymbol{U}^+_{gdq} = -L_g\frac{d\boldsymbol{I}^+_{gdq}}{dt} + \boldsymbol{E}_{gdq} \quad (11)$$

where

$$\boldsymbol{E}_{gdq} = \boldsymbol{U}^+_{sdq} - R_g\boldsymbol{I}^+_{gdq} - j\omega_1 L_g\boldsymbol{I}^+_{gdq} \quad (12)$$

where $\boldsymbol{U}$ is the voltage, $\boldsymbol{I}$ is the current, subscripts g represents the GSC, and R_g and L_g are the GSC input inductance and resistance, respectively.

In addition, the GSC active and reactive powers can be expressed as [21], [22]

$$S_g = P_g + \boldsymbol{j}Q_g = 1.5\boldsymbol{U}^+_{gdq} \times \hat{\boldsymbol{I}}^+_{gdq} \quad (13)$$

where S_g, P_g, and Q_g represent the GSC apparent, active and reactive powers, respectively

$$P_g = P_{ga} + P_{gs2}\cos(2\omega_1 t) + P_{gs2}\sin(2\omega_1 t) \quad (14a)$$

$$Q_g = Q_{ga} + Q_{gc2}\cos(2\omega_1 t) + Q_{gs2}\sin(2\omega_1 t) \quad (14b)$$

$$\begin{bmatrix} P_{ga} \\ Q_{ga} \\ P_{gc2} \\ P_{gs2} \\ Q_{gc2} \\ Q_{gs2} \end{bmatrix} = \frac{3}{2}\begin{bmatrix} U^+_{gd+} & U^+_{gq+} & U^-_{gd-} & U^-_{gq-} \\ U^+_{gq+} & -U^+_{gd+} & U^-_{gq-} & -U^-_{gd-} \\ U^-_{gd-} & U^-_{gq-} & U^+_{gd+} & U^+_{gq+} \\ U^-_{gq-} & -U^-_{gd-} & -U^+_{gq+} & U^+_{gd+} \\ U^-_{gq-} & -U^-_{gd-} & U^+_{gq+} & -U^+_{gd+} \\ -U^-_{gd-} & -U^-_{gq-} & U^+_{gd+} & U^+_{gq+} \end{bmatrix} \times \begin{bmatrix} I^+_{gd+} \\ I^+_{gq+} \\ I^-_{gd-} \\ I^-_{gq-} \end{bmatrix} \quad (14c)$$

where P_{ga}, P_{gs2}, and P_{gc2} represent the average, sine and cosine components of the GSC active power, and Q_{ga}, Q_{gs2}, and Q_{gc2} represent the average, sine and cosine components of the GSC reactive power, respectively.

According to Fig. 1, when the power loss in both the RSC and GSC is ignored, the power flowing into the dc capacitor can be expressed as

$$P_{\mathrm{dc}} = V_{\mathrm{dc}}I_{\mathrm{dc}} = P_g - P_r = P_g - (P_e - P_s) \quad (15)$$

where $P_e = P_s + P_r$ refers to the electromagnetic power, and P_r refers to the rotor power delivered from the GSC to the RSC.

It can be seen that not only the GSC power oscillations but also the power flow between the RSC and GSC can lead to the dc voltage fluctuates.

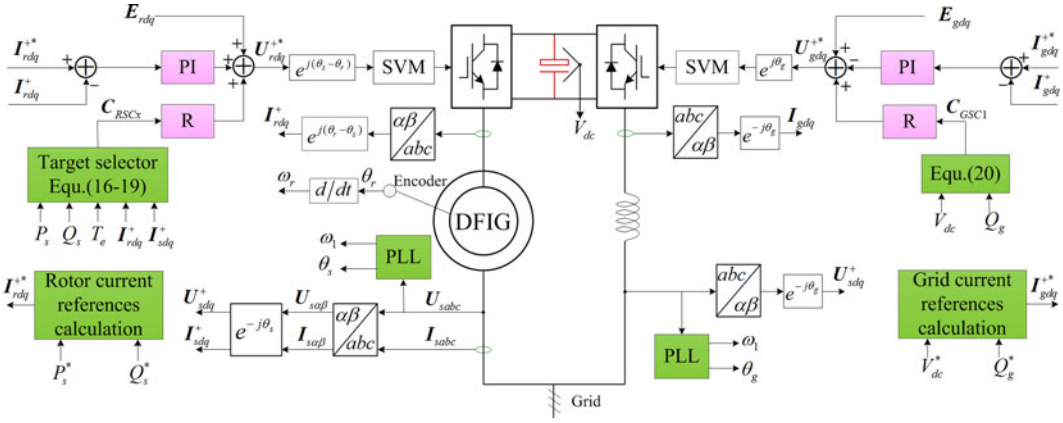

Fig. 3. Schematic diagram of the proposed control strategy for the DFIG system under network unbalance.

III. Proposed Control Strategy of the DFIG System

A. General Description

In order to avoid the complex reference calculation and sequential decomposition, Fig. 3 presents the overall schematic diagram of the proposed control scheme based on the resonant feedback compensators to implement the independent operation of the RSC and GSC. As can be seen, the proposed control strategy consists of two regulators: 1) a current PI controller; and 2) a resonant feedback compensator. The control strategy is implemented in the positive sequence voltage oriented dq^+ reference frame, where the fundamental frequency components behave as dc signals, and the negative sequence components are converted into ac signals pulsating at $2\omega_1$. In Fig. 3, the PI controllers are used to regulate dc signals, and the resonant feedback compensators, consisting of resonant regulators, as illustrated in [12] and [18], can provide an infinite gain at the double fundamental frequency. It should be noted that the resonant regulators are sensitive to frequency variations, which may degrade the control performance on the frequency variation condition. An adaptive resonant regulator was proposed in [23] and [24], in which the resonant frequency can be updated based on the frequency information detected by the phase-locked loop (PLL). Besides, a resonant-based PLL, as shown in [18] and [25], was introduced to achieve an accurate and rapid track for the network frequency and phase angular under unbalanced grid voltage conditions.

For the RSC, the PI controllers are used to regulate the average stator active and reactive power and the resonant feedback compensators are designed to achieve four different control targets, i.e., balanced stator current, sinusoidal rotor current, smooth stator active and reactive powers, and constant generator torque. The measured currents and the calculated powers and torque can be directly set as the input of the resonant feedback compensators. Thus, the sequential decompositions and the complex calculations for the negative sequence rotor current references in the proposed control strategy can be avoided.

For the GSC, the PI controllers are employed to regulate the GSC average active and reactive powers for a constant dc voltage, while the resonant feedback compensators are used to reduce the dc voltage fluctuates and remove the GSC reactive power oscillations. The dc voltage $V_{\rm dc}$ and the GSC reactive power Q_g are directly used as the input of the resonant feedback compensators. As can be seen, no power information needs to be transferred from the RSC to the GSC in this proposed control strategy. Thus, an independent operation of the RSC and GSC can be obtained for DFIG systems under unbalanced grid voltage conditions.

B. Selectable Control Targets

There are seven signals in the RSC, i.e., P_s, Q_s, T_e, I_{sd}^+, I_{sq}^+, I_{rd}^+, and I_{rq}^+. Thus, the RSC can be controlled to achieve one of the following control targets [6], [18]:

Target I: Sinusoidal rotor current with less rotor power losses.

Target II: Balanced stator current to ensure balanced heating on the stator windings.

Target III: Smooth stator output active and reactive power feed to the grid.

Target IV: Constant electromagnetic torque to reduce the mechanical stress, and no oscillations in the stator reactive power, simultaneously.

For *Target I*, the input reference of the resonant feedback compensators in the RSC can be written as

$$\boldsymbol{C}_{\rm RSC1} = C_{\rm RSC1\_d} + jC_{\rm RSC1\_q} = -I_{rd}^+ - jI_{rq}^+. \tag{16}$$

For *Target II*, the input reference of the resonant feedback compensators in the RSC can be written as

$$\boldsymbol{C}_{\rm RSC2} = C_{\rm RSC2\_d} + jC_{\rm RSC2\_q} = I_{sd}^+ + jI_{sq}^+. \tag{17}$$

For *Target III*, since the regulation of active and reactive powers can be achieved by controlling the *dq* components of the rotor currents, the smooth active and reactive powers are selected as the control target, which is similar to [18]. The input reference of the resonant feedback compensators in the RSC can be written as

$$\boldsymbol{C}_{\rm RSC3} = C_{\rm RSC3\_d} + jC_{\rm RSC3\_q} = P_s - jQ_s. \tag{18}$$

While for *Target IV*, since the *d*-axis rotor current refers to the active (torque) power components, in order to reduce the torque ripples, the torque can replace the active power in (18) as

the controlled variable of the resonant feedback compensators. Besides, in order to smooth the reactive power, the reactive power is still directly controlled by the compensators. Thus, the input reference of the resonant feedback compensators in the RSC can be written as

$$\boldsymbol{C}_{\mathrm{RSC4}} = C_{\mathrm{RSC4\_}d} + jC_{\mathrm{RSC4\_}q} = T_e - jQ_s. \quad (19)$$

Similar to the RSC, there are five controllable signals in the GSC, i.e., P_g, Q_g, V_{dc}, I_{gd}^{+}, and I_{gq}^{+}. Since the GSC can remain a constant dc-link voltage and a unity power factor operation by regulating the *d*-axis and *q*-axis currents, the control target for GSC can be designed to suppress the dc voltage fluctuates and remove the GSC reactive power oscillations at the double grid frequency. Thus, the dc-link voltage and the reactive power can be directly controlled by the resonant compensators. Then, the input reference of the resonant feedback compensators in the GSC can be expressed as

$$\boldsymbol{C}_{\mathrm{GSC1}} = C_{\mathrm{GSC1\_}d} + jC_{\mathrm{GSC1\_}q} = V_{\mathrm{dc}} + jQ_g. \quad (20)$$

Accordingly, the RSC can achieve the different control targets by simply switching the different input references of the resonant compensators on the basis of (16), (17), (18), and (19). However, these four control targets are exclusive and cannot be implemented at the same time. In GSC control, the dc-link voltage and the GSC reactive power can remain constant regardless of the selections of the different control targets for the RSC. Finally, the independent operation of DFIG's RSC and GSC can be achieved with no additional hardware and no information exchanges between these two converters.

For the DFIG systems, the selection of the control targets is highly relied on the operational requirements of the generator and the network. For instance, from the viewpoint of the grid, the sinusoidal and balanced stator current contributes to improve the power quality of the point of the common coupling, while from the viewpoint of the generator, the torque ripples are required to be reduced so as to extend the mechanical components lifetime. Thus, the aforementioned control targets are equally important, which can be adopted for different demands under unbalanced grid voltage conditions.

C. System Implementation

According to Fig. 3, the rotor voltage $\boldsymbol{U}_{rdq}^{+*}$ consists of three parts: $\boldsymbol{U}_{rdq}^{PI}$, $\boldsymbol{U}_{rdq}^{R}$, and $\boldsymbol{E}_{rdq}$. Thus, the commanded rotor voltage reference in the dq^{+} reference frame can be represented as

$$\begin{aligned}\boldsymbol{U}_{rdq}^{+*} &= \boldsymbol{U}_{rdq}^{PI} + \boldsymbol{U}_{rdq}^{R} + \boldsymbol{E}_{rdq} \\ &= G_{PI1}(\mathrm{s})(\boldsymbol{I}_{\mathrm{rdq}}^{+*} - \boldsymbol{I}_{\mathrm{rdq}}^{+}) + \mathrm{G_{R1}(s)}\,\boldsymbol{C}_{\mathrm{RSCx}} + \boldsymbol{E}_{\mathrm{rdq}} \quad (21)\end{aligned}$$

where superscript $*$ stands for the reference value, $\boldsymbol{C}_{\mathrm{RSC}x}$ is the input reference according to (16)–(19), $\boldsymbol{U}_{rdq}^{PI}$ is the output of the PI controller, and $\boldsymbol{U}_{rdq}^{R}$ is the output of the resonant feedback compensator for the RSC

$$G_{\mathrm{PI1}}(s) = k_{p1} + k_{i1}/s \quad (22)$$

$$G_{R1}(s) = 2\omega_{c1}s \cdot k_{r1}/(s^2 + 2\omega_{c1}s + (2\omega_1)^2) \quad (23)$$

where ω_{c1} is the cut-off frequency, and k_{p1}, k_{i1}, and k_{r1} are the proportional, integral, and resonant parameters for the RSC, respectively.

Then, the commanded rotor voltage is transferred to the rotor stationary reference frame and written as

$$\boldsymbol{U}_{r\alpha\beta}^{*} = \boldsymbol{U}_{rdq}^{+*} e^{j(\theta_s - \theta_r)} \quad (24)$$

where θ_s and θ_r refer to the stator voltage angle and the rotor angle, respectively.

Similar to the RSC, the controlled voltage of the GSC can be calculated as

$$\begin{aligned}\boldsymbol{U}_{gdq}^{+*} &= -\boldsymbol{U}_{gdq}^{PI} + \boldsymbol{U}_{gdq}^{R} + \boldsymbol{E}_{gdq} \\ &= -C_{\mathrm{PI2}}(s)\left(\boldsymbol{I}_{gdq}^{+*} - \boldsymbol{I}_{gdq}^{+}\right) + C_{R2}(s)\,\boldsymbol{C}_{\mathrm{GSC1}} + \boldsymbol{E}_{gdq} \quad (25)\end{aligned}$$

where $\boldsymbol{C}_{\mathrm{GSC1}}$ is the input reference according to (20), $\boldsymbol{U}_{gdq}^{PI}$ is the output of the PI controller, and $\boldsymbol{U}_{gdq}^{R}$ is the output of the resonant feedback compensators for the GSC

$$G_{\mathrm{PI2}}(s) = k_{p2} + k_{i2}/s \quad (26)$$

$$G_{R2}(s) = 2\omega_{c2}s \cdot k_{r2}/(s^2 + 2\omega_{c2}s + (2\omega_1)^2) \quad (27)$$

where ω_{c2} is the cut-off frequency, k_{p2}, k_{i2}, and k_{r2} are the proportional, integral, and resonant parameters for the GSC, respectively.

As to the GSC, the controlled voltage is transferred to the stationary reference frame as

$$\boldsymbol{U}_{g\alpha\beta}^{*} = \boldsymbol{U}_{gdq}^{+*} e^{j\theta_g} \quad (28)$$

where θ_g refers to the GSC voltage angle.

Finally, on the basis of the modulated voltage reference, shown in (24) and (28), a space vector modulation is applied to produce the required switching signals for the RSC and GSC, respectively.

IV. Control Performance Analysis

In the proposed control strategy, the resonant feedback compensators are added to the current control loop so as to achieve the aforementioned control targets, which has an impact on the control performance, including the rejection capabilities of the selected control targets to the unbalanced voltage disturbances and the dynamic responses of the rotor currents to the commanded values. Thus, the rejection capabilities and the dynamic responses of the proposed control strategy under unbalanced grid voltage conditions are quantitatively analyzed in this section.

A. Rejection Capability

Based on (1)–(3), the stator flux linkage in the positive synchronous dq^{+} reference frame can be expressed as

$$\boldsymbol{\psi}_{sdq}^{+} = \frac{1}{s + j\omega_1}\boldsymbol{U}_{sdq}^{+} - \frac{R_s}{s + j\omega_1}\boldsymbol{I}_{sdq}^{+} \quad (29)$$

$$\boldsymbol{I}_{sdq}^{+} = \frac{1}{L_s}\boldsymbol{\psi}_{sdq}^{+} - \frac{L_m}{L_s}\boldsymbol{I}_{rdq}^{+}. \quad (30)$$

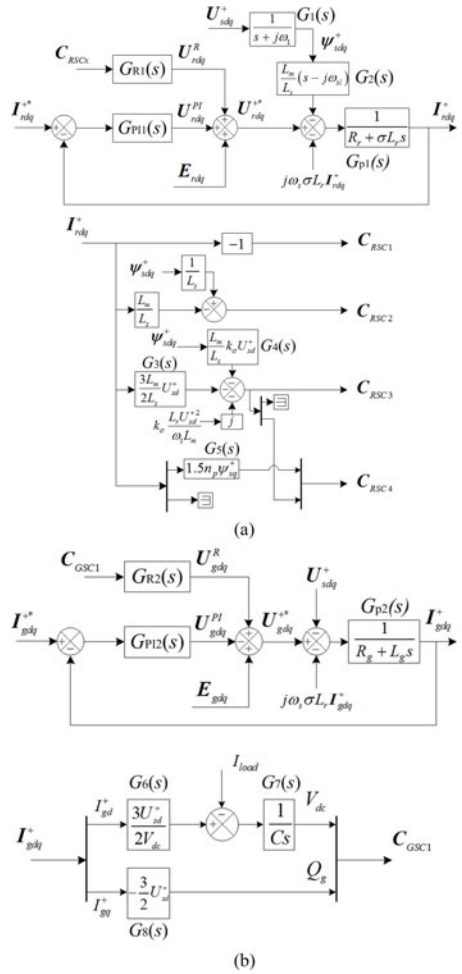

Fig. 4. Block diagram of the proposed control strategy: (a) RSC and (b) GSC.

If the stator resistance is neglected, (29) can be simplified as

$$\boldsymbol{\psi}^{+}_{sdq} = \frac{1}{s + j\omega_1}\boldsymbol{U}^{+}_{sdq}. \tag{31}$$

When the stator voltage is aligned with the *d*-axis of the dq^+ reference frame, the deferential of the stator flux will be 0. Then, the stator voltage can be written as

$$\boldsymbol{U}^{+}_{sdq} = j\omega_1\boldsymbol{\psi}^{+}_{sdq} = \left|U^{+}_{sd}\right| = -\omega_1\psi^{+}_{sq}. \tag{32}$$

Fig. 4(a) and (b) presents the block diagram of the proposed control strategy for the RSC and GSC on the basis of (5), (7), (9), (11), (13), (30), and (31), where C represents the capacitance of the dc capacitor $G_{p1}(s) = 1/(R_r + \sigma L_r s)$, $G_{p2}(s) = 1/(R_g + L_g s)$, $G_1(s) = 1/(s + j\omega_1)$, $G_2(s) = (s + j\omega_{sl})L_m/L_s$, $G_3(s) = 1.5U^{+}_{sd}L_m/L_s$, $k_\sigma = 1.5L_m/(L_sL_r - L^2_m)$, $G_4(s) = k_\sigma U^{+}_{sd}L_m/L_s$, $G_5(s) = 1.5n_p\psi^{+}_{sq} = -1.5n_pU^{+}_{sd}\omega_1$, $G_6(s) = 1.5U^{+}_{sd}/V_{\rm dc}$, $G_7(s) = 1/(Cs)$, and $G_8(s) = 1.5U^{+}_{sd}$.

Since the *d*-axis stator voltage U^{+}_{sd} contains both the positive and the negative sequence fundament components and the *q*-axis stator voltage is approximately 0, the *d*-axis average value (the positive sequence component) and *q*-axis stator voltage can be removed to simplify the expressions in the analysis, which means that the *d*-axis negative sequence voltage can be regarded as the main voltage disturbances. Thus, the overall closed-loop transfer function in the RSC control is given by

$$\boldsymbol{C}_{\mathrm{RSC}x} = H_{\mathrm{RSC}x}(s)\cdot\boldsymbol{I}^{+*}_{rdq} + F_{\mathrm{RSC}x}(\mathrm{s})\cdot\mathrm{U}^{+}_{\mathrm{sd}-} \tag{33}$$

where $x = 1, 2, 3,$ and4 represents the different control targets, $H_{\mathrm{RSC}x}(\mathrm{s})$ is the transfer function from the commanded rotor current $\boldsymbol{I}^{+*}_{rdq}$ to the controlled variable $\boldsymbol{C}_{\mathrm{RSC}x}$, and $F_{\mathrm{RSC}x}(\mathrm{s})$ is the transfer function from the grid voltage disturbance U^{+}_{sd-} to the controlled variables $\boldsymbol{C}_{\mathrm{RSC}x}$.

As can be seen, the controlled variables $\boldsymbol{C}_{\mathrm{RSC}x}$ are determined not only by the rotor current reference $\boldsymbol{I}^{+*}_{rdq}$ but also by the voltage disturbance U^{+}_{sd-}. $H_{\mathrm{RSC}x}(\mathrm{s})$ mainly represents the dynamic response of the rotor current and $F_{\mathrm{RSC}x}(\mathrm{s})$ refers to the rejection capability to voltage disturbances.

For *Target I*, i.e., $x = 1$, based on Fig. 4(a), the following transfer functions $H_{\mathrm{RSC1}}(\mathrm{s})$ and $F_{\mathrm{RSC1}}(\mathrm{s})$ can be given by:

$$H_{\mathrm{RSC1}}(s) = \frac{\boldsymbol{C}_{\mathrm{RSC1}}}{\boldsymbol{I}^{+*}_{rdq}} = \frac{G_{\mathrm{PI1}}(s)G_{p1}(s)}{1 + G_{\mathrm{PI1}}(s)G_{p1}(s) + G_{R1}(s)G_{p1}(s)} \tag{34a}$$

$$F_{\mathrm{RSC1}}(s) = \frac{\boldsymbol{C}_{\mathrm{RSC1}}}{U^{+}_{sd-}} = \frac{-G_1(s)G_2(s)G_{p1}(s)}{1 + G_{\mathrm{PI1}}(s)G_{p1}(s) + G_{R1}(s)G_{p1}(s)}. \tag{34b}$$

As with *Target II*, i.e., $x = 2$, from Fig. 4(a), the transfer functions $H_{\mathrm{RSC2}}(\mathrm{s})$ and $F_{\mathrm{RSC2}}(\mathrm{s})$ can be written as (35a) and (36b).

$$H_{\mathrm{RSC2}}(s) = \frac{\boldsymbol{C}_{\mathrm{RSC2}}}{\boldsymbol{I}^{+*}_{rdq}} = \frac{G_{\mathrm{PI1}}(s)G_{p1}(s)L_m/L_s}{1 + G_{\mathrm{PI1}}(s)G_{p1}(s) + G_{R1}(s)G_{p1}(s)L_m/L_s} \tag{35a}$$

$$F_{\mathrm{RSC2}}(s) = \frac{\boldsymbol{C}_{\mathrm{RSC2}}}{U^{+}_{sd-}} = \frac{G_1(s)/L_s + G_1(s)G_{\mathrm{PI1}}(s)G_{p1}(s)/L_s + G_1(s)G_2(s)G_{p1}(s)L_m/L_s}{1 + G_{\mathrm{PI1}}(s)G_{p1}(s) + G_{R1}(s)G_{p1}(s)L_m/L_s} \tag{35b}$$

$$H_{\mathrm{RSC3}}(s) = \frac{\boldsymbol{C}_{\mathrm{RSC3}}}{\boldsymbol{I}^{+*}_{rdq}} = \frac{G_{\mathrm{PI1}}(s)G_{p1}(s)G_3(s)}{1 + G_{\mathrm{PI1}}(s)G_{p1}(s) + G_3(s)G_{R1}(s)G_{p1}(s)} \tag{36a}$$

$$F_{\mathrm{RSC3}}(s) = \frac{\boldsymbol{C}_{\mathrm{RSC3}}}{U^{+}_{sd-}} = \frac{G_1(s)G_2(s)G_3(s)G_{p1}(s) - G_1(s)G_4(s) - G_1(s)G_4(s)G_{\mathrm{PI1}}(s)G_{p1}(s)}{1 + G_{\mathrm{PI1}}(s)G_{p1}(s) + G_3(s)G_{R1}(s)G_{p1}(s)} \tag{36b}$$

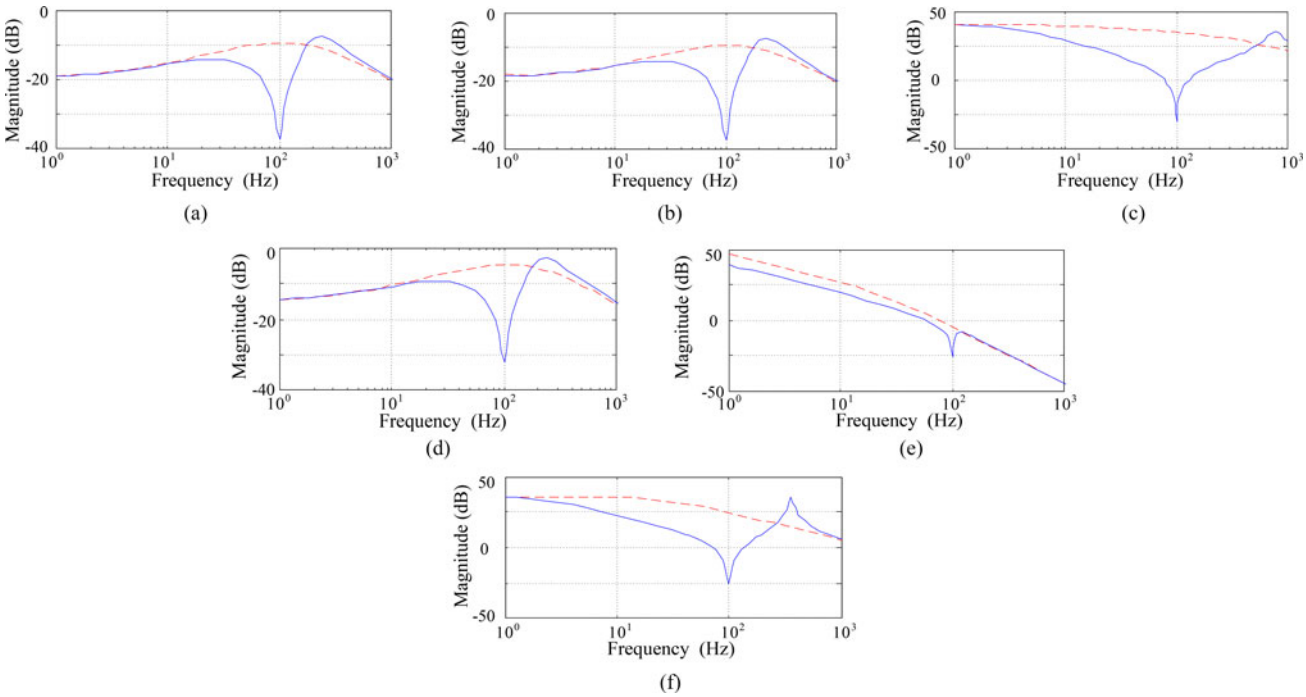

Fig. 5. Rejection capability to grid voltage disturbances. [$k_{p1}=1$, $k_{i1}=1$, $k_{r1}=15$, $k_{p2}=2$, $k_{i2}=1$, $k_{r2}=30$, $\omega_{c1}=\omega_{c2}=15$ rad/s, and $\omega_1=50\pi$ rad/s.] (a) Magnitude response of $F_1(s)$, (b) magnitude response of $F_2(s)$, (c) magnitude response of $F_3(s)$, (d) magnitude response of $F_{41}(s)$, (e) magnitude response of $H_{11}(s)$, and (f) magnitude response of $H_{12}(s)$. [Dash: resonant feedback compensators disabled; solid: resonant feedback compensators enabled.]

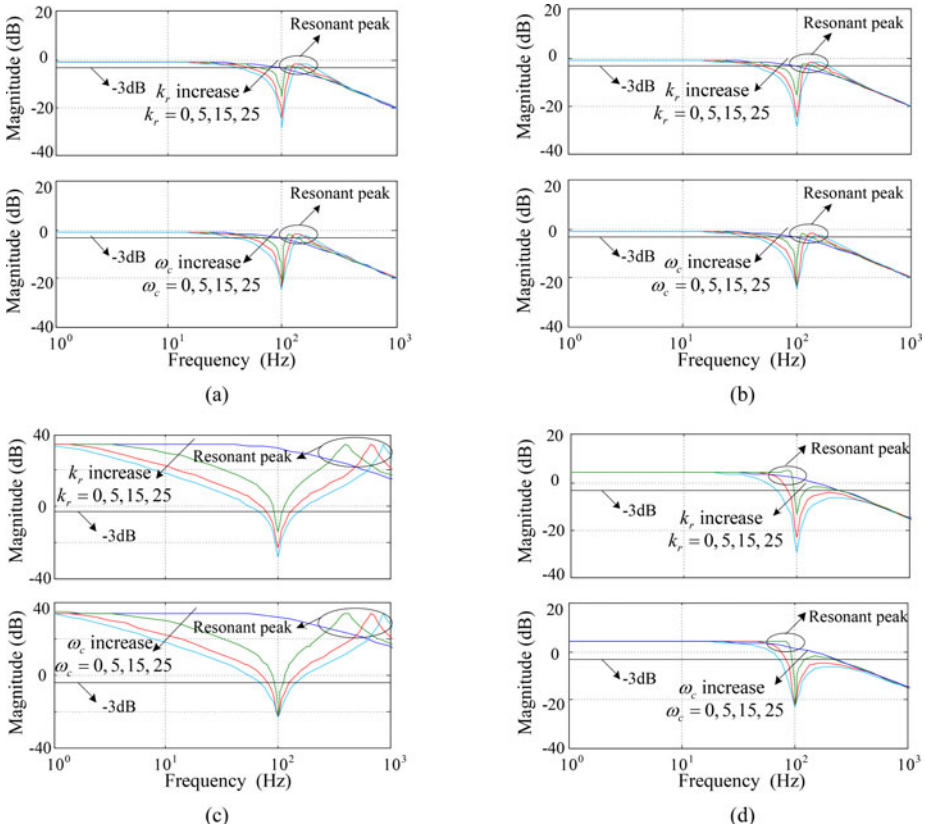

Fig. 6. Amplitude responses of $H_{\mathrm{RSC}x}(s)$ ($x=1,2,3,$ and 4) with k_r and ω_c variations. [$k_{p1}=1, k_{i1}=1, k_{r1}=15, \omega_{c1}=15$ rad/s, and $\omega_1=50\pi$ rad/s.] (a) *Target I*, (b) *Target II*, (c) *Target III*, and (d) *Target IV*.

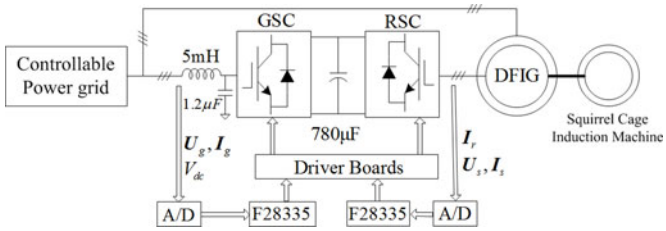

Fig. 7. Configuration of the experimental system.

TABLE I
PARAMETERS OF THE TESTED DFIG

Rated power	1.5 kW	Rated voltage	150 V
Rated frequency	50 Hz	DC voltage	300 V
Stator/rotor turns ratio	0.33	R_s	1.01 Ω
R_r	0.88 Ω	L_m	90.1 mH
$L_{\sigma s}$	3.0 mH	$L_{\sigma r}$	3.0 mH

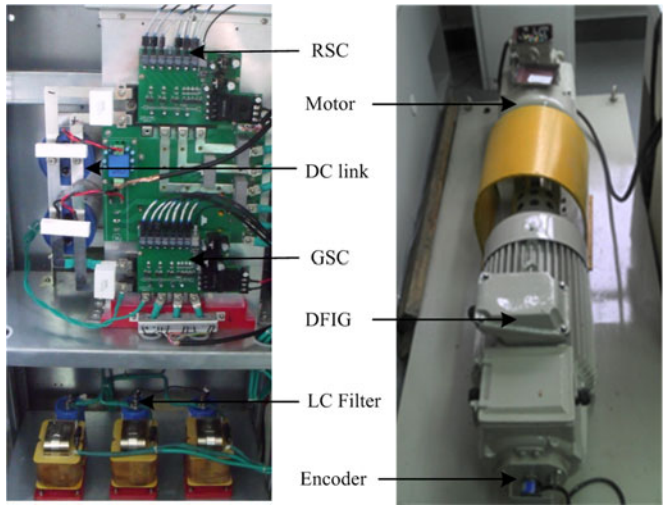

Fig. 8. Experimental setup of the tested DFIG.

While for *Target III*, i.e., $x = 3$, the transfer functions $H_{\mathrm{RSC3}}(\mathrm{s})$ and $F_{\mathrm{RSC3}}(\mathrm{s})$ can be obtained by (36a) and (36b).

As for *Target IV*, i.e., $x = 4$, the transfer functions $H_{\mathrm{RSC4}}(\mathrm{s})$ and $F_{\mathrm{RSC4}}(\mathrm{s})$ for the stator reactive power Q_s are the same as those of *Target III*, shown in (36a) and (36b). The transfer functions from the commanded rotor current and the grid voltage disturbance to the torque T_e can be expressed as

$$H_{\mathrm{RSC4}}(s) = \frac{T_e}{\boldsymbol{I}_{rdq}^{+*}} = \frac{G_{\mathrm{PI1}}(s)G_{p1}(s)G_5(s)}{1 + G_{\mathrm{PI1}}(s)G_{p1}(s) + G_5(s)G_{R1}(s)G_{p1}(s)} \tag{37a}$$

$$F_{\mathrm{RSC4}}(s) = \frac{T_e}{U_{sd-}^{+}} = \frac{-G_1(s)G_2(s)G_5(s)G_{p1}(s)}{1 + G_{\mathrm{PI1}}(s)G_{p1}(s) + G_{R1}(s)G_{p1}(s)}. \tag{37b}$$

Similar to the RSC, the controlled variable $\boldsymbol{C}_{\mathrm{GSC1}}$ is determined by both the grid current reference $\boldsymbol{I}_{gdq}^{+*}$ and the grid voltage disturbance U_{sd-}^{+}. Since the bandwidth of the dc voltage loop is much lower, the dc voltage loop has less impact on the 100 Hz component, which means that the dc-voltage loop can be ignored when the rejection capability of grid voltage disturbance is discussed. The overall closed-loop transfer function for GSC is shown as

$$\boldsymbol{C}_{\mathrm{GSC1}} = H_{\mathrm{GSC1}}(\mathrm{s}) \cdot \boldsymbol{I}_{\mathrm{gdq}}^{+*} + \mathrm{F}_{\mathrm{GSC1}}(\mathrm{s}) \cdot \mathrm{U}_{\mathrm{sd-}}^{+} \tag{38}$$

where $H_{\mathrm{GSC1}}(\mathrm{s})$ is the transfer function from the commanded grid current $\boldsymbol{I}_{gdq}^{+*}$ to the controlled variable $\boldsymbol{C}_{\mathrm{GSC1}}$, and $F_{\mathrm{GSC1}}(\mathrm{s})$ is the transfer function from the voltage disturbance U_{sd-}^{+} to the controlled variables $\boldsymbol{C}_{\mathrm{GSC1}}$.

In a similar way, the dynamic performance of the overall system is mainly decided by the current loop $H_{\mathrm{GSC1}}(s)$ and the rejection capability is generally determined by $F_{\mathrm{GSC1}}(s)$

$$H_{\mathrm{GSC1}}(s) = \frac{C_{\mathrm{GSC1}}}{I_{gdq}^{+*}} = \frac{G_{PI2}(s)G_{p2}(s) \cdot G_X(s)}{1 + G_{\mathrm{PI2}}(s)G_{p2}(s) + G_{R2}(s)G_{p2}(s) \cdot G_X(s)} \tag{39a}$$

$$F_{\mathrm{GSC1}}(s) = \frac{C_{\mathrm{GSC1}}}{U_{sd-}^{+}} = \frac{G_{p2}(s) \cdot G_X(s)}{1 + G_{\mathrm{PI2}}(s)G_{p2}(s) + G_{R2}(s)G_{p2}(s) \cdot G_X(s)} \tag{39b}$$

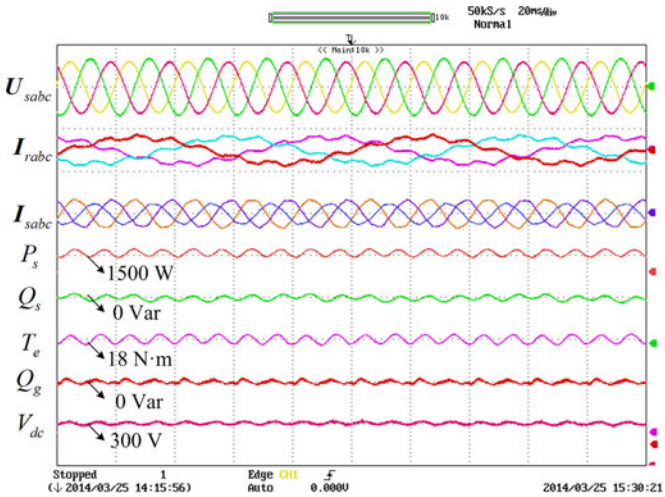

Fig. 9. Experimental results of the conventional vector control under an 80% single-phase grid voltage fault (20 ms/div). [Stator line voltage U_{sab}, U_{sbc}, and U_{sca} (300 V/div), rotor current I_{rabc} (10 A/div), stator current I_{sabc} (30 A/div), stator active power P_s (700 W/div), stator reactive power Q_s (700 Var/div), DFIG torque T_e (4 N·m/div), GSC reactive power Q_g (700 Var/div), and dc voltage V_{dc} (20 V/div).]

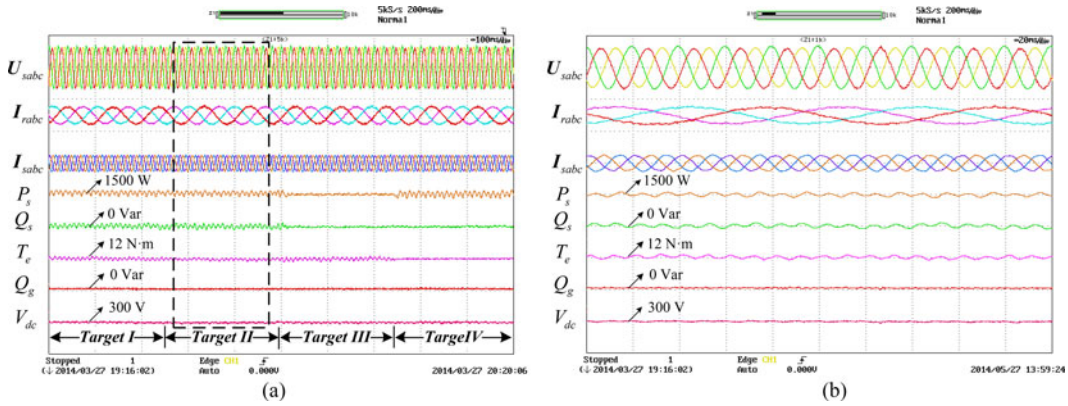

Fig. 10. Experimental results of the proposed control scheme with control targets changing under an 80% single-phase grid voltage fault. [Stator line voltage U_{sab}, U_{sbc}, and U_{sca} (300 V/div), rotor current I_{rabc} (10 A/div), stator current I_{sabc} (30 A/div), stator active power P_s (700 W/div), stator reactive power Q_s (700 Var/div), DFIG torque T_e (4 N·m/div), GSC reactive power Q_g (700 Var/div), and dc voltage $V_{\rm dc}$ (20 V/div).] (a) Full view (100 ms/div) and (b) enlarged view with Target II adopted (20 ms/div).

TABLE II
COMPARISONS AMONG SELECTABLE CONTROL TARGETS DURING NETWORK UNBALANCE

Control targets	Compensators disabled	Compensators enabled			
		Target I	Target II	Target III	Target IV
I_r ninth-order (%)	16.1	**1.5**	1.9	3.3	2.8
I_s unbalance (%)	18.1	2.8	**2.2**	3.8	4.3
P_s pulsation (%)	±8.9	±5.7	±5.1	± **0.9**	±7.1
Q_s pulsation (%)	±7.8	±5.1	±4.3	± **1.1**	±**1.2**
T_e pulsation (%)	±5.2	±2.6	±3.0	±3.7	± **0.8**
$V_{\rm dc}$ pulsation (%)	±1.2	± **0.4**			
Q_g pulsation (%)	±4.1	± **1.2**			

where $G_X(s) = G_6(s) \cdot G_7(s)$ for the dc voltage $V_{\rm dc}$, and $G_X(s) = G_8(s)$ for the GSC reactive power Q_g.

In order to achieve the selected control targets, the proposed control strategy based on the resonant feedback compensators should have enough rejection capability on negative sequence grid voltage disturbances. The rejection capabilities can be represented by the amplitude responses of $F_{\rm RSC}x({\rm s})$ ($x = 1, 2, 3,$ and 4) and $F_{\rm GSC1}(s)$. Fig. 5 presents the amplitude responses of $F_{\rm RSC}x({\rm s})$ ($x = 1, 2, 3,$ and 4) and $F_{\rm GSC1}({\rm s})$, which represent the rejection capabilities of the proposed control strategy to the grid voltage disturbance U^+_{sd-}. It can be seen from Fig. 5(a) that the magnitude response at 100 Hz is -37.2 dB with the control *Target I* with the resonant feedback compensators, whereas it is only -9.1 dB without the feedback compensator. Thus, the proposed control strategy can increase the rejection capability, resulting in the less impacts caused by the voltage imbalance on the rotor current. Fig. 5(b) and (c) exhibits similar responses as Fig. 5(a), where the magnitude responses decrease to -36.7 dB and -29.5 dB when *Target II* and *Target III* are selected, respectively. For *Target IV*, the transfer function of the negative sequence voltage U^+_{sd-} to the stator reactive power Q_s is the same as (36b) whose frequency response is given in Fig. 5(c), while the frequency response of (37b) is shown in Fig. 5(d) where the magnitude response decreases from -4.3 to -33.2 dB when the resonant feedback compensators are employed. For the GSC, Fig. 5(e) and (f) presents the magnitude responses of (39b), where $G_X(s) = G_6(s) \cdot G_7(s)$ and $G_X(s) = G_8(s)$, respectively. As can be seen, the magnitude responses decrease to –25.3 dB from -4.4 dB for the dc voltage $V_{\rm dc}$ and to -26.9 dB from 25.6 dB for the GSC reactive power Q_g, respectively. Therefore, it can be concluded that the proposed control strategy can significantly improve the rejection capabilities of the grid voltage disturbances and reduce the negative impacts on the DFIG system.

B. Dynamic Responses

It is also important to investigate the dynamic responses of rotor currents with different control targets for the proposed control strategy. Based on the analysis, it is noted that the frequency responses of $H_{\rm RSC}x({\rm s})$ or $H_{\rm GSC1}$, shown in (34a), (35a), (36a), (37a), and (39a), represent the dynamic responses of the rotor current. According to [26], the major difference among the different targets for dynamic responses analysis is highly dependent on the closed-loop gain, such as $G_3(s)$, $G_5(s)$, $G_6(s)$, $G_7(s)$, and $G_8(s)$ in Fig. 3. Since these transfer functions, (34a), (35a), (36a), (37a), and (39a), have similar expressions, for simplified analysis, the dynamic responses of the RSC are investigated in this section.

Fig. 6 presents the amplitude responses of $H_{\rm RSC}x({\rm s})$ ($x = 1, 2, 3,$ and4), representing the dynamic responses of the rotor current control loop. Note that if $k_r = 0$ or $\omega_c = 0$, it is identically to use a PI controller without resonant feedback compensators. It can be seen that these transfer functions (34a), (35a), (36a), and (37a) have similar amplitude responses as shown in Fig. 6. Thus, for simplified analysis, this section would investigate the dynamic responses with *Target IV* set for the RSC, shown in Fig. 6(d). The cut-off frequency, i.e., the minimum frequency for -3 dB, is 230, 95, 82, and 67 Hz when $k_r = 0$, 5, 15, 30, and $\omega_c = 15$ rad/s, respectively. It has the similar amplitude responses that the cut-off frequency is 230, 93, 81, and

66 Hz when $\omega_c = 0$, 5, 15, 30, and $k_r = 15$ rad/s, respectively. The conclusions can be summarized that the cut-off frequency with k_r variations is close to that with ω_c variations if k_r is approximately equal to ω_c. Besides, the settling time, which is inversely to the cut-off frequency [19], [26], might be increased with the proposed method. It should be pointed out that it has a negative impact on the dynamic performance of the rotor current responses, which is a result of the introduced those compensators.

The coefficients k_r and ω_c should be set as smaller as possible so as to reduce this negative impact. However, resonant peaks appear with a smaller k_r and ω_c, which may cause the rotor current oscillations near the resonant frequency and even cause the system to destabilize. Therefore, taking both the dynamic performance and the system stability into consideration, the coefficients k_r and ω_c can be determined to be around 15.

V. Experimental Results

Experimental tests were conducted on a laboratory setup of a 1.5 kW DFIG system, as shown in Fig. 7, where the DFIG was driven by a squirrel cage induction motor working as the wind turbine. A controllable three-phase power supply was built up to simulate the unbalanced grid voltage conditions [26]. The control strategy is implemented on the TI TMS320F28335 DSPs and the switching frequency is 10 kHz with a sampling frequency of 10 kHz. Parameters and structures of the tested DFIG are shown in Table I and Fig. 8. The stator active and reactive power into the grid were set as $P_{sa} = 1.5$ kW and $Q_{sa} = 0.0$ kVar, respectively. The dc voltage is kept at 300 V. Since the large inertia of wind turbine results in a larger mechanical time constant than the electromagnetic one and the voltage fault usually lasts for a short period of time, the rotor speed can be assumed to be fixed for the analysis in this paper. The DFIG speed was initially fixed at 800 r/min during the experimental tests, where the synchronous speed is 1000 r/min. All the waveforms are acquired by a YOKOGAWA DL750 scope reader.

Fig. 9 shows the steady performance of the conventional vector control under an 80% single-phase grid voltage fault. Note that the conventional vector control, i.e., pure PI, means that the resonant feedback compensators are disabled. As can be seen, the stator current, containing 18.1% negative sequence component, is greatly unbalanced due to the negative sequence voltage disturbances. Since the rotor speed is 800 r/min (0.8 p.u., 40 Hz), the air gap magnetic field, containing the 50 Hz component rotating in the negative direction, would result in 90 Hz $(50 + 40$ Hz) rotor current harmonic component in the rotor stationary reference frame, which can be regard as the ninth order harmonic component. This ninth harmonic content is around 16.1%. The generator torque ripples are nearly $\pm 5.2\%$. As also can be seen, the stator active and reactive powers involve 100 Hz oscillations. Furthermore, the dc voltage fluctuates are about $\pm 1.2\%$.

Fig. 10 shows the experimental results of the proposed method with different control targets applied under an 80% single-phase grid voltage fault, and the enlarged view with Target II is shown in Fig. 10(b) to give a better interpretation of the balanced stator currents on the proposed control strategy. In the RSC, the control target is switched to the next control target within 250 ms, while the GSC is controlled to maintain a constant dc voltage and remove the reactive power oscillations. It can be seen that the steady operation of RSC on the different control targets can be achieved. The dc voltage fluctuates are suppressed by the proposed method without any power information from the RSC, and the GSC reactive power oscillations are removed at the same time.

For clear comparisons, the ninth harmonic distortion of rotor current, the unbalance of stator current, the oscillating extent of the stator active and reactive powers, the torque, the GSC reactive power, and the dc voltage are summarized with the resonant feedback compensators disabled and enabled for different control targets in Table II. It is concluded that the experimental results demonstrate the availability and feasibility of the proposed control strategy with the alternative control targets under unbalanced grid voltage conditions.

Since the GSC current references are produced by the dc voltage loop, the dynamic responses of the current loop cannot be clearly seen. Thus, for simplified analysis, the performance with *Target IV* set for the RSC is tested in the following so as to compare the dynamic performance of the PI + R method [12] and the proposed method with a transient grid voltage unbalance.

Fig. 11(a) and (b) compares the dynamic performance of the PI + R method [12] and the proposed method employed with an 80% single-phase grid voltage dip. It is seen that the torque ripples can be successfully reduced to $\pm 0.9\%$ by these two control schemes. The settling time of the torque is decreased from 50 ms for the PI + R method to 20 ms for the proposed method. It is evident that the proposed method can behave much quicker with a transient voltage unbalance. The reason is that both the sequential decompositions and the reference calculations in the PI + R method [12] involve the time delay, resulting in a relatively slow dynamic performance.

Fig. 12 shows the experimental results of the DFIG operation from the subsynchronous state to the supersynchronous state with an 80% single phase fault, where the RSC and GSC is controlled to reduce the torque ripples and the dc voltage fluctuates, respectively. Furthermore, an enlarged view around the synchronous speed is shown in Fig. 12(b) to give a clear interpretation of the DFIG system performance on the proposed control strategy. During this process of the rotor speed accelerating from 800 r/min (0.8 p.u.) to 1200 r/min (1.2 p.u.), the proposed control strategy can achieve a smooth performance, where the torque and dc voltage remain nearly constant. The results verify that the proposed control strategy can provide a satisfactory dynamic response with the rotor speed changing under unbalanced grid voltage conditions.

From the experimental results, it can be clearly concluded that the selectable control targets for the RSC and GSC can be achieved under unbalanced grid voltage conditions when the resonant feedback compensators are used. It is not necessary to decompose the positive and negative sequence components and calculate the negative sequence current references. However,

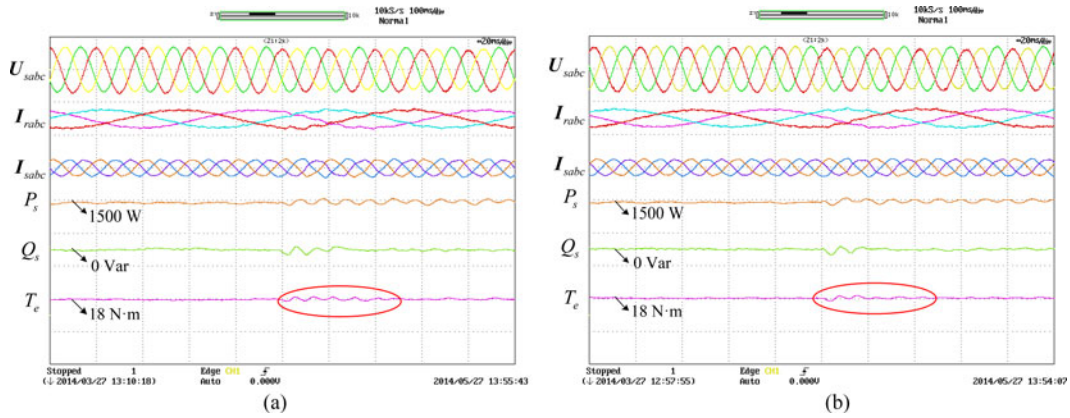

Fig. 11. Experimental results of the PI + R and the proposed control strategy for *Target IV* under an 80% single-phase grid voltage fault. [Stator line voltage U_{sab}, U_{sbc}, and U_{sca} (300 V/div), rotor current I_{rabc} (10 A/div), stator current I_{sabc} (30 A/div), stator active power P_s (700 W/div), stator reactive power Q_s (700 Var/div), and DFIG torque T_e (4 N·m/div).] (a) PI + R control (20 ms/div) and (b) proposed control (20 ms/div).

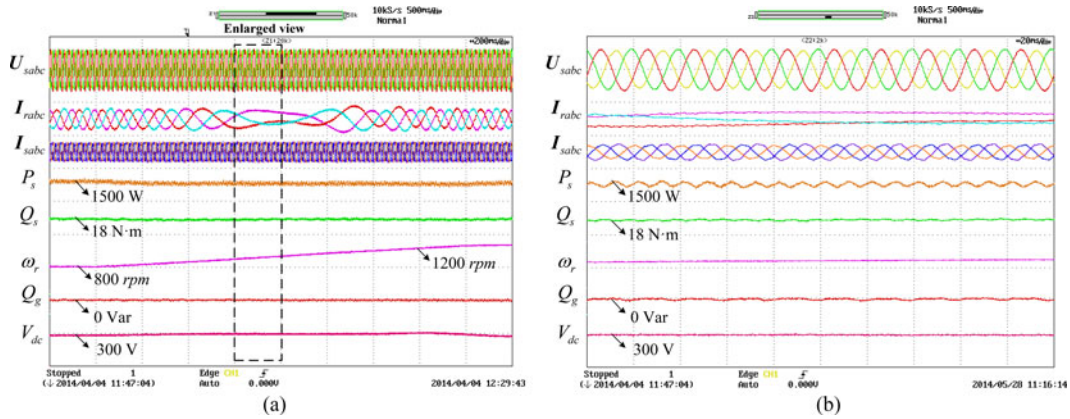

Fig. 12. Experimental results of the proposed control strategy under an 80% single-phase grid voltage fault with the speed variation. [Stator line voltage U_{sab}, U_{sbc}, and U_{sca} (300 V/div), rotor current I_{rabc} (10 A/div), stator current I_{sabc} (30 A/div), stator active power P_s (700 W/div), stator reactive power Q_s (700 Var/div), DFIG torque T_e (4 N·m/div), GSC reactive power Q_g (700 Var/div), and dc voltage $V_{\rm dc}$ (20 V/div).] (a) Full view (200 ms/div) and (b) enlarged view (20 ms/div).

these control targets are independent and exclusive, which can be achieved at the same time.

VI. Conclusion

An independent and reinforced operation for DFIG systems under unbalanced grid voltage conditions has been investigated in this study. Detailed designs of the proposed control strategy are presented. The experimental results on a laboratory setup of the 1.5 kW DFIG system validate the effectiveness of the proposed control strategy. For a clear statement, the following conclusions can be summarized:

1) An entire control scheme for both the RSC and GSC under unbalanced grid voltage conditions is presented. Four control targets for the RSC and one for the GSC are identified and achieved, respectively, where the sequential decompositions of the positive and negative sequence components are not required.
2) The proposed control strategy can provide a relatively simple implementation with less computational load and less system complexity. By this means, it is not necessary to calculate the negative current reference on the basis of the generator parameters. This advantage means that the proposed control strategy is less dependent on the generator parameters.
3) The proposed control strategy can provide an independent control for the RSC and GSC. The GSC has nothing to do with the power information from the RSC. This control strategy is much more suitable for the DFIG converters with a modular structure.

References

[1] M. Liserre, R. Cardenas, M. Molinas, and J. Rodriguez, "Overview of multi-MW wind turbines and wind parks," *IEEE Trans. Ind. Electron.*, vol. 58, no. 4, pp. 1081–1095, Apr. 2011.
[2] F. Blaabjerg and K. Ma, "Future on power electronics for wind turbine systems," *IEEE J. Emerg. Sel. Topics Power Electron.*, vol. 1, no. 3, pp. 139–152, Sep. 2013.
[3] H. Polinder, J. A. Ferreira, B. B. Jensen, A. B. Abrahamsen, K. Atallah, and R. A. McMahon, "Trends in wind turbine generator systems," *IEEE J. Emerg. Sel. Topics Power Electron.*, vol. 1, no. 3, pp. 174–185, Sep. 2013.

[4] S. Muller, M. Deicke, and R. W. De Doncker, "Doubly fed induction generator systems for wind turbines," *IEEE Ind. Appl. Mag.*, vol. 8, no. 3, pp. 26–33, May/Jun. 2002.
[5] J. Yao, H. Li, Z. Chen, X. F. Xia, X. Y. Chen, Q. Li, and Y. Liao, "Enhanced control of a DFIG-based wind-power generation system with series grid-side converter under unbalanced grid voltage conditions," *IEEE Trans. Power Electron.*, vol. 28, no. 7, pp. 3167–3181, Jul. 2013.
[6] L. Xu and Y. Wang, "Dynamic modeling and control of DFIG-based wind turbines under unbalanced network conditions," *IEEE Trans. Power Syst.*, vol. 22, no. 1, pp. 314–323, Feb. 2007.
[7] J. Lopez, E. Gubia, P. Sanchis, X. Roboam, and L. Marroyo, "Wind turbines based on doubly fed induction generator under asymmetrical voltage dips," *IEEE Trans. Energy Convers.*, vol. 23, no. 1, pp. 321–330, Mar. 2008.
[8] Y. Zhou, P. Bauer, J. A. Ferreira, and J. Pierik, "Operation of grid-connected DFIG under unbalanced grid voltage condition," *IEEE Trans. Energy Convers.*, vol. 24, no. 1, pp. 240–246, Mar. 2009.
[9] E.ON Netz GmbH. (Apr. 2006). *Grid Code for High and Extra High Voltage* [Online]. Available: http://www.eon-netz.com
[10] M. Tsili and S. Papathanassiou, "A review of grid code technical requirements for wind farms," *IET Renew. Power Gener.*, vol. 3, no. 3, pp. 308–332, Sep. 2009.
[11] C. Jauch, J. Matevosyan, T. Ackermann, and S. Bolik, "International comparison of requirements for connection of wind turbines to power systems," *Wind Energy*, vol. 8, no. 3, pp. 295–306, Jul./Sep. 2005.
[12] J. B. Hu, Y. K. He, L. Xu, and B. W. Williams, "Improved control of DFIG systems during network unbalance using PI-R current regulators," *IEEE Trans. Ind. Electron.*, vol. 56, no. 2, pp. 439–451, Feb. 2009.
[13] J. B. Hu and Y. K. He, "Reinforced control and operation of DFIG-based wind-power-generation system under unbalanced grid voltage conditions," *IEEE Trans. Energy Convers.*, vol. 24, no. 4, pp. 905–915, Dec. 2009.
[14] T. K. A. Brekken and N. Mohan, "A novel doubly-fed induction wind generator control scheme for reactive power control and torque pulsation compensation under unbalanced grid voltage conditions," in *Proc. Power Electron. Spec. Conf.*, vol. 2, 2003, pp. 760–764.
[15] T. K. A. Brekken and N. Mohan, "Control of a doubly fed induction wind generator under unbalanced grid voltage conditions," *IEEE Trans. Energy Convers.*, vol. 22, no. 1, pp. 129–135, Mar. 2007.
[16] J. B. Hu, Y. K. He, and H. Nian, "Enhanced control of DFIG-used back-to-back PWM VSC under unbalanced grid voltage conditions," *J. Zhejiang Univ. Sci. A*, vol. 8, no. 8, pp. 1330–1339, Aug. 2007.
[17] L. Xu, "Coordinated control of DFIG's rotor and grid side converters during network unbalance," *IEEE Trans. Power Electron.*, vol. 23, no. 3, pp. 1041–1049, May 2008.
[18] P. Zhou, Y. He, and D. Sun, "Improved direct power control of a DFIG-based wind turbine during network unbalance," *IEEE Trans. Power Electron.*, vol. 24, no. 11, pp. 2465–2474, Nov. 2009.
[19] C. Liu, D. Xu, N. Zhu, F. Blaabjerg, and M. Chen, "DC-voltage fluctuation elimination through a DC-capacitor current control for DFIG converters under unbalanced grid," *IEEE Trans. Power Electron.*, vol. 28, no. 7, pp. 3206–3218, Jul. 2013.
[20] L. Xu, "Enhanced control and operation of DFIG-based wind farms during network unbalance," *IEEE Trans. Energy Convers.*, vol. 23, no. 4, pp. 1073–1081, Dec. 2008.
[21] J. B. Hu and Y. K. He, "Multi-frequency proportional-resonant (MFPR) current controller for PWM VSC under unbalanced supply conditions," *J. Zhejiang Univ. Sci. A*, vol. 8, no. 10, pp. 1527–1531, Oct. 2007.
[22] L. Xu, B. R. Andersen, and P. Cartwright, "VSC transmission system operating under unbalanced network conditions—Analysis and control design," *IEEE Trans. Power Del.*, vol. 20, no. 1, pp. 427–434, Jan. 2005.
[23] P. Rodriguez, A. Luna, R. S. Munoz-Aguilar, I. Etxeberria-Otadui, R. Teodorescu, and F. Blaabjerg, "A stationary reference frame grid synchronization system for three-phase grid-connected power converters under adverse grid conditions," *IEEE Trans. Power Electron.*, vol. 27, no. 1, pp. 99–112, Jan. 2012.
[24] C. J. Liu, F. Blaabjerg, W. J. Chen, and D. H. Xu, "Stator current harmonic control with resonant controller for doubly fed induction generator," *IEEE Trans. Power Electron.*, vol. 27, no. 7, pp. 3207–3220, Jul. 2012.
[25] H. Nian, Y. P. Song, P. Zhou, and Y. K. He, "Improved direct power control of a wind turbine driven doubly fed induction generator during transient grid voltage unbalance," *IEEE Trans. Energy Convers.*, vol. 26, no. 3, pp. 976–986, Sep. 2011.
[26] H. Nian and Y. P. Song, "Direct power control of doubly fed induction generator under distorted grid voltage," *IEEE Trans. Power Electron.*, vol. 29, no. 2, pp. 894–905, Feb. 2014.

Heng Nian (M'09) received the B.Eng. and M.Eng. degrees from the Hefei University of Technology, Hefei, China, and the Ph.D. degree from Zhejiang University, Hangzhou, China, in 1999, 2002, and 2005, respectively, all in electrical engineering.

From 2005 to 2007, he was a Postdoctoral Researcher with the College of Electrical Engineering, Zhejiang University, where since 2007 he has been an Associate Professor. His current research interests include the optimal design and operation control for the wind power generation system.

Peng Cheng was born in Chaoyang, China. He received the B.Sc. degree from the College of Electrical Engineering, Zhejiang University, Hangzhou, China, in July 2011, where he is currently working toward the Ph.D. degree.

His current research interests include motor control with power electronics devices in renewable-energy conversion, particularly the control and operation of doubly fed induction generators for wind power generation.

Z. Q. Zhu (M'90–SM'00–F'09) received the B.Eng. and M.Sc. degrees from Zhejiang University, Hangzhou, China, in 1982 and 1984, respectively, and the Ph.D. degree from the University of Sheffield, Sheffield, U.K., in 1991, all in electrical and electronic engineering.

Since 1988, he has been with the University of Sheffield, where he is currently a Professor of electrical machines and control systems, the Head of the Electrical Machines and Drives Research Group, and the Academic Director of Sheffield Siemens Wind Power Research Centre. His current major research interests include design and control of permanent-magnet brushless machines and drives for applications ranging from automotive to renewable energy.